EINDHOVEN UNIVERSITY OF TECHNOLOGY

Influence of the size, order and topology of mesopores in bifunctional Pd-containing acidic SBA-15 and M41S catalysts for n-hexadecane hydrocracking

Citation for published version (APA):
Romero, D. E., Rigutto, M., & Hensen, E. J. M. (2022). Influence of the size, order and topology of mesopores in bifunctional Pd-containing acidic SBA-15 and M41S catalysts for n-hexadecane hydrocracking. *Fuel Processing Technology*, *232*, Article 107259. https://doi.org/10.1016/j.fuproc.2022.107259

Document license:
CC BY

DOI:
10.1016/j.fuproc.2022.107259

Document status and date:
Published: 01/07/2022

Document Version:
Publisher's PDF, also known as Version of Record (includes final page, issue and volume numbers)

Please check the document version of this publication:

• A submitted manuscript is the version of the article upon submission and before peer-review. There can be important differences between the submitted version and the official published version of record. People interested in the research are advised to contact the author for the final version of the publication, or visit the DOI to the publisher's website.
• The final author version and the galley proof are versions of the publication after peer review.
• The final published version features the final layout of the paper including the volume, issue and page numbers.

Link to publication

General rights
Copyright and moral rights for the publications made accessible in the public portal are retained by the authors and/or other copyright owners and it is a condition of accessing publications that users recognise and abide by the legal requirements associated with these rights.

• Users may download and print one copy of any publication from the public portal for the purpose of private study or research.
• You may not further distribute the material or use it for any profit-making activity or commercial gain
• You may freely distribute the URL identifying the publication in the public portal.

If the publication is distributed under the terms of Article 25fa of the Dutch Copyright Act, indicated by the "Taverne" license above, please follow below link for the End User Agreement:

www.tue.nl/taverne

Take down policy
If you believe that this document breaches copyright please contact us at:

openaccess@tue.nl

providing details and we will investigate your claim.

Download date: 05. Oct. 2023

Fuel Processing Technology 232 (2022) 107259

Contents lists available at ScienceDirect

Fuel Processing Technology

journal homepage: www.elsevier.com/locate/fuproc

Influence of the size, order and topology of mesopores in bifunctional Pd-containing acidic SBA-15 and M41S catalysts for n-hexadecane hydrocracking

Douglas E. Romero [a], Marcello Rigutto [b], Emiel J.M. Hensen [a,*]

[a] Inorganic Materials and Catalysis, Department of Chemical Engineering and Chemistry, Eindhoven University of Technology, P.O. Box 513, 5600 MB Eindhoven, the Netherlands

[b] Shell Global Solutions International B.V., P.O. Box 38000, 1030 BN Amsterdam, the Netherlands

ARTICLE INFO

Keywords:
Mesoporous silica
SBA-15
M41S
N-hexadecane
Hydrocracking

ABSTRACT

The catalytic performance in n-hexadecane hydrocracking of a set of bifunctional catalysts composed of acidic mesoporous silicas, i.e., SBA-15, MCM-41, MCM-48, and amorphous silica-alumina (ASA), and Pd as acid and (de)hydrogenation components, respectively, was investigated. The selectivity to cracked products and the occurrence of secondary cracking depended on the pore topology, acidity, and Pd dispersion. The Si/Al ratio and the mesopore order of SBA-15 were modified by changing the pH in the synthesis step. Al was introduced in the M41S materials by post-synthesis grafting. All materials including ASA exhibited low acidity compared to crystalline zeolites. Increasing Al content led to a decrease of the order of mesopores. Secondary cracking of n-hexadecane was more pronounced for catalysts containing long one-dimensional cylindrical pores (SBA-15 and MCM-41) in comparison with catalysts containing three-dimensional ordered (MCM-48) or disordered (ASA) mesopores. The selectivity difference is attributed to differences in residence time of intermediates in the mesopores. The distance between acid sites located in mesopores and Pd nanoparticles primarily located outside these pores also influences the product distribution. Ideal hydrocracking operation is approached for ASA, MCM-48, and SBA-15 prepared at a high pH containing disordered mesopores.

1. Introduction

Hydrocracking of long-chain paraffins into transportation fuels constitutes one of the most versatile processes in the petrochemical industry. It involves the cracking and isomerization of hydrocarbons and is primarily used to obtain high-quality middle distillates. Hydroisomerization refers to processes in which the branching occurs with very limited cracking. It is used to improve the cold-flow properties of diesel fuel and to obtain high-octane gasoline blending components and lube oils with good cold-flow properties. These hydroconversion processes follow a bifunctional mechanism in which a dehydrogenation/hydrogenation (metal or metal sulphide sites) function is combined with acid-catalyzed isomerization and cracking functions [1].

The hydrocarbon product distribution depends amongst other on the balance and (spatial) intimacy of these two functions, giving rise to "ideal" vs. "non-ideal" hydrocracking. Shape selectivity refers to the influence of the pore size in which the cracking reactions take place [2–4]. In the classical interpretation of the hydrocracking mechanism [5,6], n-alkane is dehydrogenated on a metal site to the corresponding n-alkene, which desorbs and diffuses to Brønsted acid sites where it further reacts via carbenium ion chemistry. This includes skeletal rearrangements and β-scission (carbon-carbon bond cleavage) reactions. The rate of the ß-scission step depends on the degree of isomerization previously attained, i.e., alkylcarbenium intermediates with a larger number of branches will crack faster. The product of the primary β-scission reaction can undergo additional transformations, including a secondary ß-scission event if diffusion of the intermediate to hydrogenation sites is too slow. Thus, desorption, diffusion and the relative location of the hydrogenation to the acid function play a role in the distribution of the cracked products. Typical hydrogenation functions include metals such as Pt, Pd and Ni, because they provide sufficient dehydrogenation activity, although with a tendency to paraffin hydrogenolysis in the case of Ni and Pt [7,8]. The acidic component is usually provided by a zeolite or amorphous silica-alumina. While these solids can also serve as a support

* Corresponding author.
E-mail address: e.j.m.hensen@tue.nl (E.J.M. Hensen).

https://doi.org/10.1016/j.fuproc.2022.107259
Received 3 January 2022; Received in revised form 13 March 2022; Accepted 20 March 2022
Available online 2 April 2022
0378-3820/© 2022 The Authors. Published by Elsevier B.V. This is an open access article under the CC BY license (http://creativecommons.org/licenses/by/4.0/).

for the hydrogenation function, composite catalysts may also contain other supports such as γ-alumina on which the metal phase can be dispersed. Strongly acidic zeolites are favoured for hydrocracking purposes, while supports with a limited acidity are more selective towards isomerization. Zeolites contain acid sites located in micropores with dimensions in the order of the size of hydrocarbons to be converted, inducing specific shape selectivity. Amorphous silica-alumina typically has larger mesopores, which are arranged in a random manner compared to the micropore topology of zeolites. Ordered mesoporous silicas such as MCM-41, which are acidic by introducing aluminum in the amorphous silica network, have also been used for hydrocracking purposes to establish the effect of a uniform pore size and ordered pore arrangement on cracking reactions [9]. The industrial relevance of such ordered mesoporous materials is, however, limited because of the high cost associated with the organic templates used in their preparation as well as their low hydrothermal stability. While MCM-41 presents a tubular pore system, MCM-48 exhibits a three-dimensional system of mesopores. SBA-15 is another ordered mesoporous silica with a similar hexagonal structure as MCM-41 but with larger pores, thicker silica walls and, therefore, higher hydrothermal stability [10,11].

In the present work, we compared the performance of different ordered mesoporous silicas (SBA-15, MCM-41, MCM-48) and amorphous silica-alumina (ASA), which contains disordered mesopores, as acidic supports for the hydroconversion of n-hexadecane (n-C_{16}) in a trickle-bed microflow reactor. The aim was to understand the influence of the size and order of the (*meso*)pores on the product distribution. Acidity was introduced into the ordered mesoporous silicas by aluminum either in the synthesis step or by post-synthesis alumination of the calcined silica materials. The acidic, textural and morphological properties of the porous materials were characterized by elemental analysis, X-ray diffraction (XRD), N_2 porosimetry, transmission electron microscopy (TEM), solid state NMR spectroscopy and IR spectroscopy. The Pd metal phase was characterized by H_2 chemisorption and IR spectroscopy of adsorbed CO.

2. Experimental methods

2.1. Synthesis of ordered mesoporous silicas

A range of SBA-15 samples with a target Si/Al ratio of 20 were synthesized under acidic conditions, employing HCl solutions with pH 1.0, 1.5, 1.6, 1.7, 2.0, and 2.5. In a typical procedure based on a literature recipe [12], a solution A was prepared by dissolving 2 g Pluronic P123 in 70 ml in the acid solution followed by stirring at 313 K for 6 h. A second solution B was obtained by dissolving 0.22 g aluminum triisopropoxide and 3.2 ml tetramethylorthosilicate (TMOS) in 5 ml of the acid solution, followed by stirring at room temperature for 2 h. Solution B was then added to solution A, followed by further stirring at 313 K for 20 h. The resulting suspension was transferred to a Teflon-lined stainless-steel autoclave, which was then sealed and heated at 373 K for 48 h. The resulting materials are denoted according to the pH of the starting solution as P1.0, P1.5, P1.6, P1.7, P2.0 and P2.5. An siliceous MCM-41 sample was prepared according to literature [13], by dissolving 3.8 g tetramethyl ammonium hydroxide solution (TMAOH, 25% wt in water) and 4.6 g cetyltrimethyl ammonium bromide (CTAB) in 34.1 g water. After stirring at 308 K for 1 h, 3.0 g fumed silica was added and the gel was further stirred at room temperature for 20 h. The gel was transferred to a Teflon-lined stainless-steel autoclave and heated at 423 K for 48 h. A siliceous MCM-48 sample prepared according to Ref. [14] was synthesized by dissolving 2.14 g fumed silica in 30 g a 10 wt% cetyltrimethylammonium hydroxide solution in water (CTAOH). After stirring at room temperature for 2 h, the gel was transferred to a Teflon-lined stainless-steel autoclave and heated at 408 K for 24 h. After the hydrothermal synthesis step, the solids were filtrated and washed with deionized water. All these samples were dried overnight at 373 K and the template was removed in a next step by calcination at 773 K for 10 h (SBA-15 samples) and 823 K for 6 h (MCM-41 and MCM-48 samples).

2.2. Alumination of silicas

The siliceous MCM-41 and MCM-48 samples were aluminated by a dry alumination method [15,16]. For this purpose, 2.0 g calcined MCM-41 was dispersed in 50 ml of dry n-hexane. Solutions containing 0.17 g (0.11 g) aluminum isopropoxide in 150 ml of n-hexane were prepared to obtain materials with Si/Al ratios of 40 (60) (denoted hereafter as M41–40 and M41–60). The MCM-41 suspension was added to the aluminum-containing solution and the mixture was stirred at room temperature for 24 h. For MCM-48, 1 g silica was directly added to a solution containing 0.06 g of aluminum isopropoxide in 50 ml of n-hexane and the resulting dispersion was further stirred at room temperature for 24 h to obtain a Si/Al ratio of 60 (sample M48–60). The solids were recovered by filtration and washed with n-hexane. The samples were dried overnight at 373 K and subsequently calcined at 823 K for 4 h. A commercial ASA (amorphous silica alumina 75/25 *w*/w from supplier JGC) was used as received.

2.3. Characterization

The elemental composition of the solids was determined by ICP-OES (Spectro CirosCCD ICP optical emission spectrometer). X-ray diffraction (XRD) patterns were recorded on a Bruker D2 Endeavor diffractometer using Cu Kα radiation with a scanning speed of 0.02 °/s in the 2θ range of 0–10 °. N_2 adsorption and desorption isotherms were measured at 77 K on a Micromeritics TriStar II 3020 instrument. For this purpose, 100 mg of the sample were transferred in a glass sample tube, followed by drying at 393 K in a N_2 flow overnight.

IR spectra were recorded in the range of 4000–400 cm^{-1} using a Bruker Vertex V70v Fourier-transform infrared spectrometer. CO IR spectroscopy was used to probe the acid and metal sites. To evaluate the acidity, the sample was cooled to ~90 K and CO was introduced into the cell via a sample loop connected to a six-port valve. After each CO dosage, a spectrum was recorded. For metal site determination, a similar procedure was followed with the difference that the samples were reduced before IR characterization carried out at 303 K. Reduction was performed in pure hydrogen by heating to 673 K at a rate of 3 K/min, followed by a dwelling time of 1 h. The sample was evacuated until a residual pressure of 1×10^{-5} mbar was reached. The sample was cooled to 303 K and CO was introduced into the cell.

For IR spectroscopy of adsorbed pyridine, the probe molecule was introduced from an ampoule at its vapor pressure at room temperature. After exposure of the dehydrated sample to pyridine for 10 min, the cell was evacuated and a spectrum was recorded. Further spectra were recorded after outgassing for 1 h at 423 K, 573 K and 773 K. The acidic properties were also characterized by H/D exchange of the hydroxyl groups with deuterated benzene (C_6D_6) followed by IR spectroscopy. In a typical experiment based on literature [17], C_6D_6 was dosed to the dehydrated sample compartment from a manifold until a pressure of 10 mbar is reached, which corresponds to a total amount of 0.33 mmol (sample density 7.5 mg/cm^2). The sample was exposed to C_6D_6 for 10 s, followed by evacuation for 1 h. The final pressure was lower than 10^{-6} mbar. Then, a spectrum of the partially exchanged sample was recorded. This sequence was automatically repeated with exposure times of 30 s, 5 min, 10 min, 20 min, and 30 min at 303 K, 30 min at 323 K, 30 min at 373 K, 30 min at 423 K and 30 min at 523 K.

^{27}Al nuclear magnetic resonance (NMR) spectra were recorded on a 11.7 T Bruker DMX500 NMR spectrometer operating at 132 MHz. Transmission electron microscopy (TEM) images were taken using a FEI Tecnai 20 at an acceleration voltage of 200 kV. The samples were suspended in ethanol and dispersed over a holey Cu grid coated with carbon film.

H_2 uptake measurements were used to determine the metal surface area in reduced catalysts. Typically, 50 mg sample was loaded in a

quartz reactor. Prior to dosing, samples were reduced in flowing H_2 (1 h, 673 K, 3 K/min), evacuated at 723 K for 1 h to remove chemisorbed hydrogen and cooled to 353 K under vacuum. Chemisorption analysis was then carried out at 353 K.

2.4. Catalytic activity measurements

The solid acids were loaded with 1 wt% Pd by wet impregnation with an aqueous $Pd(NH_3)_4(NO_3)_2$ solution. The resulting samples were calcined at 723 K in flowing air for 4 h. In order to perform n-C_{16} hydroconversion activity measurements, the catalyst was dried in the reactor at 1 bar and 473 K for 1 h in a He flow and subsequently reduced at 60 bar in a H_2 flow. During reduction, the temperature was increased at a rate of 3 K/min to 673 K followed by an isothermal period of 1 h. Then, the temperature of the catalyst bed was lowered to 473 K and the packed bed was wetted by maintaining a liquid flow rate of 1 ml/min for 10 min. The reactor was operated at a H_2/n-C_{16} molar ratio of 20 and a weight hourly space velocity (WHSV) of 10 $g_{n\text{-}C16}\ g_{cat}^{-1}\ h^{-1}$. The reaction temperature was increased stepwise and the reaction was equilibrated for 3 h before product sampling. The reactor effluent was analyzed by gas chromatograph equipped with an RTX-1 column and a flame ionization detector. The identification of isomers and cracked fractions was done in accordance to the elution sequence reported in the literature [18]. Due to the large number of products observed, monobranced (ex. 3-methylpentadecane or 4-methylpentadecane) and multibranched (ex. 2,13-dimethyltetradecane or trimethyltridecanes) C_{16} isomers were lumped as 'C_{16} isomers', while the fractions including normal paraffins from methane to n-pentadecane and their corresponding isomers were lumped as 'cracked products'.

3. Results and discussion

3.1. Structure and morphology

The composition of the calcined materials as determined by ICP analysis is presented in Table 1. The Si/Al ratios of the SBA-15 samples are lower with increasing pH of the synthesis solution. Small-angle XRD patterns (Fig. 1, left) show that SBA-15 samples with a low Al content obtained at a pH below 2 exhibit three well-resolved peaks related to 100, 110 and 200 planes, characteristic of the *p6mm* hexagonal symmetry of SBA-15 [11]. From the a_0 value of about 12 nm and the pore size distribution derived from porosimetry, a wall thickness between 2.4 nm and 4 nm was determined for these samples [19]. The absence of low-angle features in the silica materials prepared at pH 2 and higher show that the samples with a higher Al content do not contain ordered mesopores. The isoelectric point of silica is around 2. This means that, when SBA-15 is prepared at a pH of 2 or higher, there are not enough positively charged protonated hydroxyl groups that can interact with the poly(ethylene oxide) groups of the Pluronic P123 mesoporogen. As a consequence, mainly disordered silica is obtained as discussed before [20,21]. In general, a pH lower than 1.5 is needed to obtain a sufficiently charged silica surface to assemble a well-ordered silica-polymer mesophase using Pluronic P123 [22].

The MCM-41 sample with a low Al content (M41–60) shows the relevant diffraction peaks related to 100, 110, 200 and 210 planes of the *p6mm* hexagonal symmetry [13,23]. At higher Al content (sample M41–40), the intensity of these peaks is lower, indicating a lower order of mesopores. This phenomenon, which has been mentioned in the literature [24,25], is likely related to a decrease in the long-range order at higher Al loading, although the local hexagonal order of the material is largely maintained. The XRD pattern of M48–60 contains the typical diffraction peaks associated with 211, 220 and 420 planes, which is due to the *Ia3d* cubic structure [16]. As expected, the walls of the MCM-41 (1.3 nm) and MCM-48 (1.2 nm) samples are thinner than those of SBA-15. The physisorption isotherms of these samples were of type IV, typical of mesoporous materials (Fig. 2). The presence of sharp pore filling/emptying steps within a narrow p/p_0 range for SBA-15 and MCM-41 materials is indicative of uniform cylindrical pores, presenting an H1 hysteresis loop [12,23]. The MCM-41 samples prepared using CTAB as structure-directing agent normally have pores in the range of 2–5 nm with relatively closed hysteresis loops in comparison to the ones observed in SBA-15 materials in which capillary condensation is more pronounced due to the larger pore size [26,27].

The NL-DFT method was used to calculate the pore size distribution from the adsorption branch of the isotherms (Fig. S1 of supporting information). Increasing pore sizes were obtained for SBA-15 samples containing more Al. For example, the Si-SBA-15 sample (P1.0) has an average pore size of 7.9 nm. Addition of more Al to the gel to arrive 0.25 wt% (P1.5) caused the pores to swell to a size of 8.8 nm. A higher Al content (i.e., comparing 0.48 wt% and 0.80 wt%, samples P1.6 and P1.7) led to pores larger than 9 nm. This behavior has been observed before [19] and can be explained by the swelling properties of the micellar arrays by isopropanol obtained by hydrolysis of the Al precursor. A comparison of the textural properties of M41–40 and M41–60 (Table 1, Fig. S1) shows that alumination by the dry-grafting method causes the pores to shrink, decreasing the pore volume and surface area [28]. The MCM-48 sample shows a sharp pore filling step in the p/p_0 range from 0.20 to 0.35, suggesting a good mesostructural order with uniform pore channels and a relatively narrow pore size distribution [29]. A weak hysteresis loop between p/p_0 values of 0.40 and 0.80 points

Table 1
Al content, Si/Al ratio, fraction of framework Al, and textural properties of the acidic support materials.

Sample	pH	Al (% wt)[a]	Si/Al[a]	Al^{IV},[b]	Al^{VI},[b]	a_o (nm)[c]	*SA* (m^2/g)[d]	V_p (cm^3/g)[e]	D_p (nm)[f]	*w* (nm)[g]
P1.0	1.0	0	∞	–	–	12.0	885	0.83	7.9	4.1
P1.5	1.5	0.25	193	0.54	0.46	12.0	987	1.25	8.8	3.2
P1.6	1.6	0.48	97	0.64	0.36	11.8	908	1.13	9.2	2.6
P1.7	1.7	0.80	60	0.66	0.34	12.6	952	1.11	9.1	3.5
P2.0	2.0	1.23	39	0.66	0.34	–	958	1.28	9.1	–
P2.5	2.5	1.70	20	0.64	0.36	–	878	1.27	9.4	–
M41–40	–	0.93	52	0.64	0.36	–	1089	1.15	3.8	–
M41–60	–	0.78	62	0.62	0.38	5.5	884	1.02	4.2	1.3
M48–60	–	0.71	68	0.55	0.45	8.2	1195	1.05	2.9	1.2
ASA	–	2.39	3	n.d.	n.d.	–	430	0.74	–	–

[a] From ICP measurements.
[b] Al^{IV} = Area of Al^{IV}/(Area of Al^{IV} + Area of Al^{VI}). Al^{VI} = Area of Al^{VI}/(Area of Al^{IV} + Area of Al^{VI}). Area of Al^{IV} determined by integration of ^{27}Al NMR signal between 30 and 100 ppm. Area of Al^{VI} determined by integration of ^{27}Al NMR signal between 30 and − 50 ppm.
[c] $a_o = 2d_{100}/3^{1/2}$ (MCM-41, SBA-15); $a_o = 2d_{211}*6^{1/2}$ (MCM-48).
[d] Brunauer-Emmett-Teller (BET) surface area (p/p_0 = 0.05–0.25).
[e] Total pore volume determined at p/p_0 = 0.97.
[f] From N_2 physisorption using the NL-DFT method.
[g] $w = a_o - D_p$ (MCM-41, SBA-15); $w = a_o/3.092 - D_p/2$ (MCM-48).

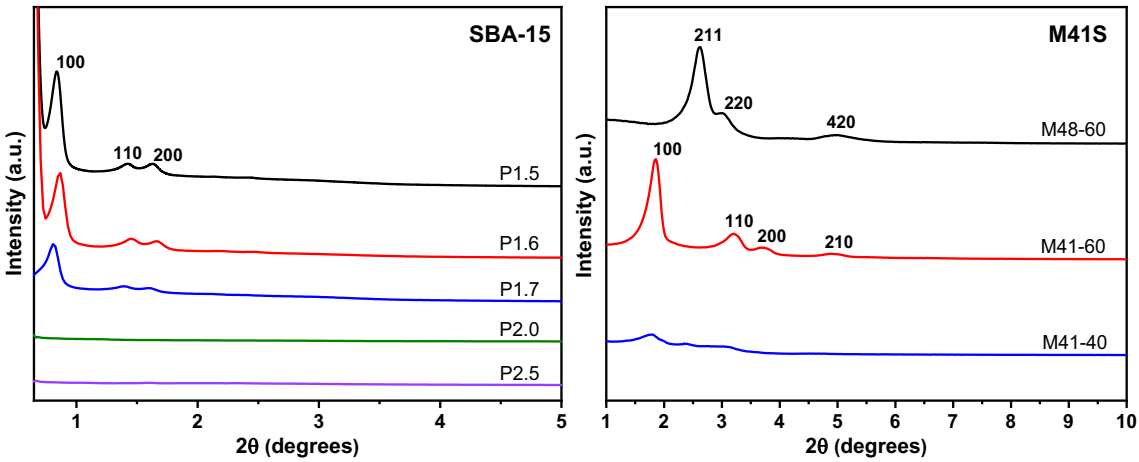

Fig. 1. Small-angle XRD patterns of the calcined SBA-15 (left) and MCM-41/MCM-48 (right) materials (relevant reflections of the SBA-15 and M41S structures marked).

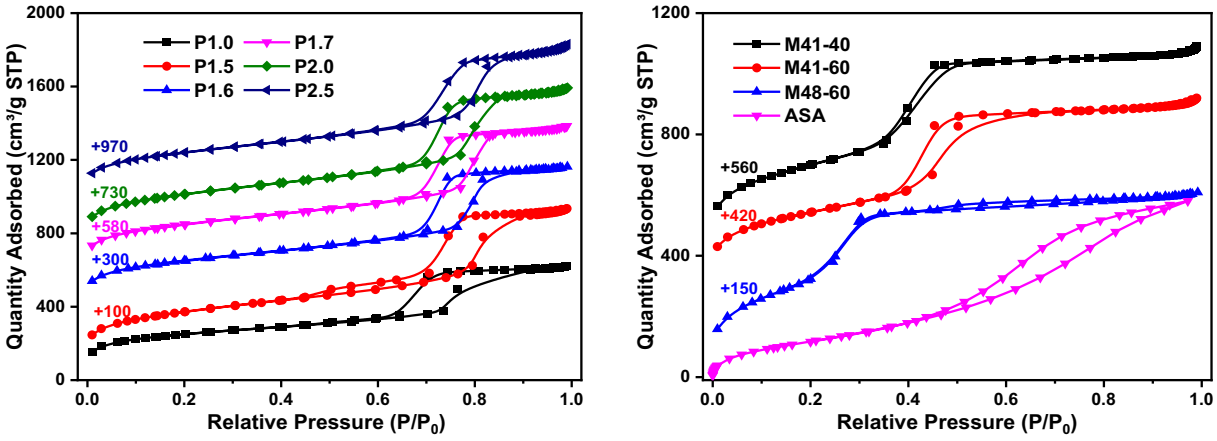

Fig. 2. N_2 physisorption isotherms of calcined SBA-15 (left) and MCM-41/MCM-48 (right) samples. The right panel also includes the isotherm for ASA.

to capillary condensation in secondary mesopores arising from interparticle voids [30,31]. ASA, on the other hand, exhibits an isotherm with a broad pore filling profile and a hysteresis loop in the p/p_0 range from 0.43 and 1.00, which points to pores with broad size distribution as might be expected for this type of material. The pore size distribution ranges between 2 nm and 60 nm. The much wider pores result in lower surface area and pore volume in comparison to the ordered mesoporous samples.

Fig. 3 shows representative TEM images of the mesoporous materials. The images of samples P1.5, P1.6 and P1.7 confirm a morphology consisting of regular arrays of long cylindrical channels with a uniform hexagonal arrangement along the 100 plane [12,19,32]. The mesopores are not always running in a straight way through the matrix, but they can be curved to some extent. It is also evident that sample P1.7 (Fig. 4-f) exhibits regions where the characteristic features of SBA-15 are not present, indicating a lower order of the mesopores. In spite of the absence of low-angle features in the XRD patterns, samples P2.0 and P2.5 still preserve areas with uniform pores, which are consistent with the shapes of the adsorption isotherms presented in Fig. 2 and the uniform pore size distribution observed in Fig. S1. Nevertheless, the ordered hexagonal pore system is not present to the same extent as in the other SBA-15 materials prepared at lower pH. The M41–60 sample (Fig. 3-i) displays mesopores arranged in a hexagonal honeycomb-like structure, separated by thin amorphous silica pore walls [9,33].

The image of M41–40 shown in Fig. 3-j reveals that an irregular pore arrangement of cylindrical pores can still be observed, making apparent that the incorporation of aluminum into the framework affects the long-range order of the mesopores without affecting the mesoporous nature of the material [34]. MCM-48 (Fig. 3 k-l) has been reported to present uninterrupted channels along the 100 and 111 planes, but due to changes in the curvature of the material, no channels are observed in other directions such as the 110 plane [35].

The coordination environment of aluminum in the samples was investigated by ^{27}Al MAS NMR spectroscopy (Fig. 4). The spectra are characterized by a strong peak at 55 ppm due to tetrahedrally coordinated aluminum (Al^{IV}), indicating that a significant fraction of Al atoms has been grafted as tetrahedral species on the silica of the mesoporous materials. Part of these Al species may also be in the silica network due to the calcination procedure. An additional weak feature at 0 ppm can be associated to Al species in octahedral coordination (Al^{VI}) [33]. The Al speciation for the investigated materials is given in Table 1. The Al^{IV} fraction of all the samples lies between 0.54 and 0.66. As expected, no Al was incorporated in the SBA-15 samples synthesized at pH 1 [36].

3.2. Acidity characterization

IR spectroscopy of adsorbed CO at 90 K was used to determine the density and strength of Brønsted acid sites (BAS). The carbonyl stretching region of IR spectra for samples M48–60 (left) and P1.7 (right) is displayed in Fig. 5. The band at 2138 cm^{-1} belongs to

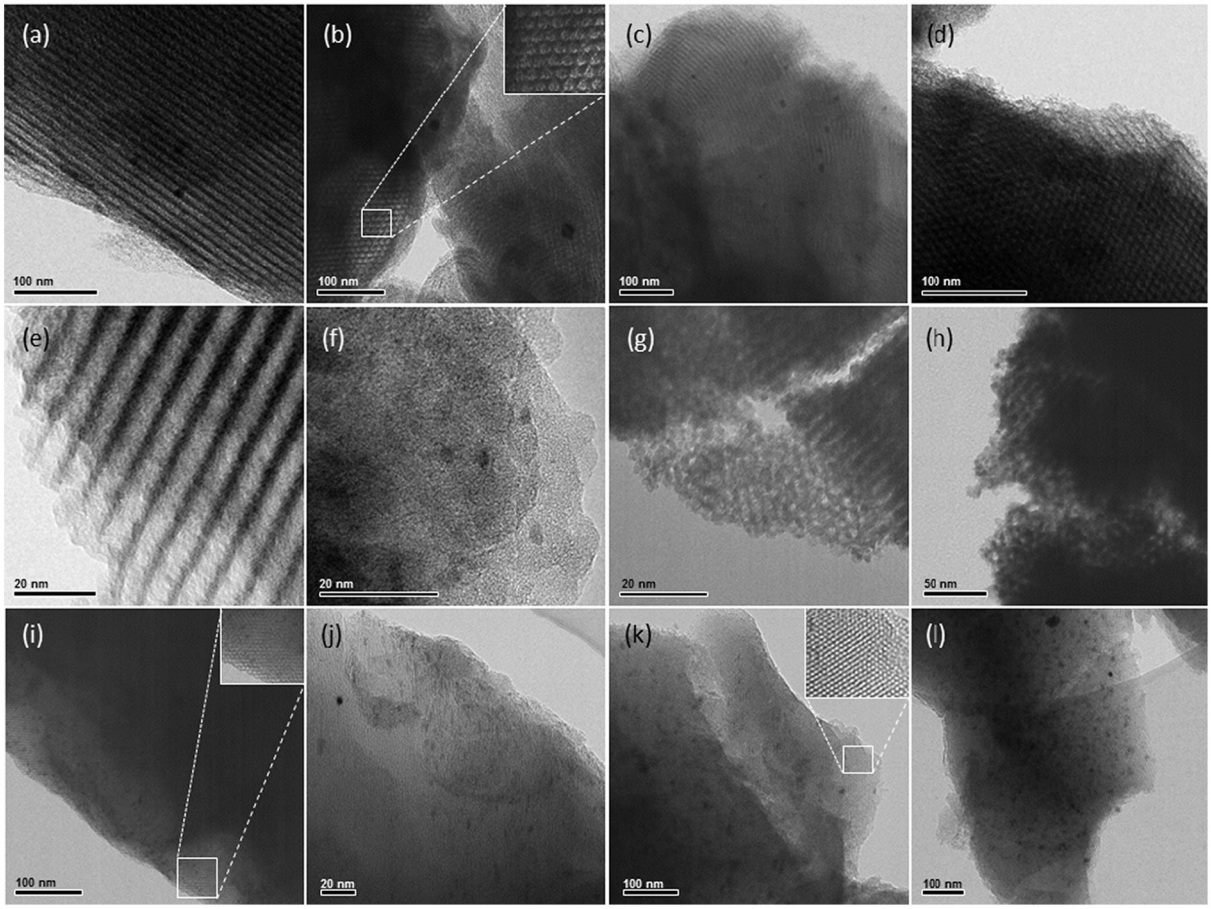

Fig. 3. Representative TEM images of Pd loaded mesoporous silicas: (a-b) P1.5, (c-d) P1.6, (e-f) P1.7, (g) P2.0, (h) P2.5, (i) M41–60, (j) M41–40, and (k-l) M48–60.

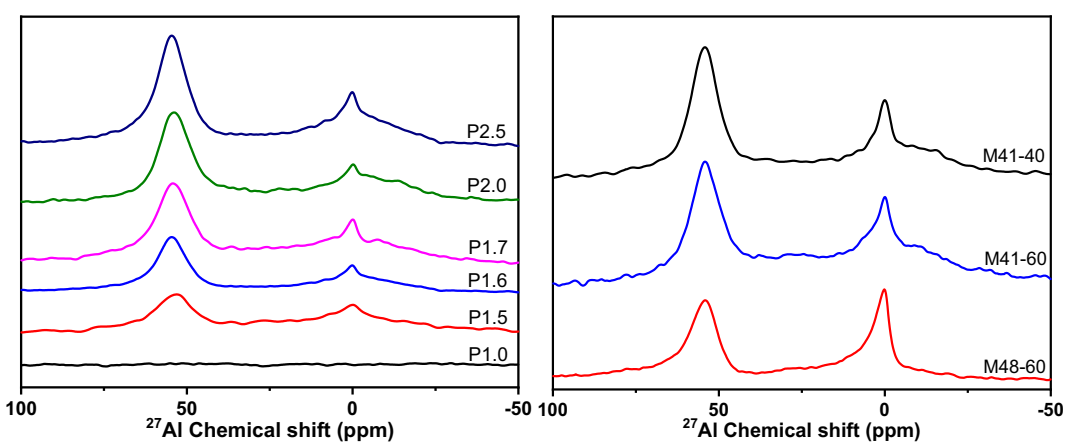

Fig. 4. ^{27}Al MAS NMR spectra of the calcined mesoporous materials.

physisorbed CO and the one at 2156 cm^{-1} to CO coordinating to silanol groups. Brønsted acid sites (BAS) are represented by the band at 2174 cm^{-1}. Previous work has shown that this feature is a composite of bands due to a small amount of strong BAS at 2178 cm^{-1} and a larger amount of relatively weak BAS at 2172 cm^{-1} [37]. The weak feature observed at 2190 cm^{-1} is due to weak Lewis acid sites (LAS).

Deconvolution of the peak related to BAS according to a procedure described before [38] provides an estimate of the population of these two types of BAS [39,40]. Spectra of sample P1.7 at different CO coverages are given in the supporting information. Table 2 shows that the concentration of strong BAS increases with the Al content for the SBA-15 samples. The concentrations are however very low, explaining why CO-perturbed bridging OH groups at 3300 cm^{-1} cannot observed as a distinct feature for these samples [41]. IR spectra of adsorbed pyridine followed by evacuation at 423 K, 573 K and 773 K for the SBA-15 samples are presented in Fig. 6. The bands at 1545 cm^{-1} and 1455 cm^{-1} are assigned to pyridine adsorbed on, respectively, BAS and LAS, while the band at 1490 cm^{-1} can be associated with both types of adsorbed pyridine [41,42]. The acid site concentrations derived from pyridine IR are listed in Table 2. In general, the SBA-15 samples contain

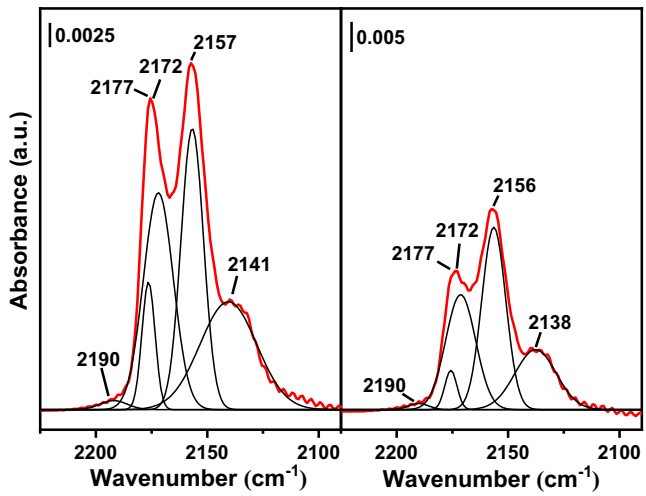

Fig. 5. Deconvolution of the carbonyl stretching region of IR spectra of CO adsorbed on M48–60 (left) and P1.7 (right) at 77 K after saturation of the band due to strong BAS.

small amounts of BAS in accordance with the results obtained with CO IR spectroscopy. The absence of a feature related to BAS in these spectra recorded after evacuation at 773 K shows that only minor amounts of strong BAS are present in these samples.

To determine the presence of small amounts of strong BAS in a semi-quantitative manner, H/D exchange of OH groups with deuterated benzene was followed by IR spectroscopy. The OD region for samples M48–60 (left), P1.7 (center) and the OH region for P1.7 (right) are shown in Fig. 7. All the samples present a clear peak at 2683 cm^{-1}, corresponding to selective H/D exchange of bridging hydroxyl groups, even at short exposure times (10–30 s) for materials with high aluminum content.

These samples also display an additional feature at 2632 cm^{-1}, related with the exchange of bridging OH groups exhibiting additional electrostatic interactions to adjacent oxygens [43] or bridging OH interacting instead with hydrogen from residual water [17], which become predominant at increasing exposure temperatures for all the samples. The H/D exchange of weak silanol groups was also observed as a band developing at 2752 cm^{-1}. The analogous bands of bridging OH groups located in the OH region at 3638 cm^{-1} and 3570 cm^{-1} [44] cannot be observed in the IR spectra because of the broad OH band at 3746 cm^{-1} (Fig. 6 top, right). The concentration of strong BAS was determined from the spectra after H/D exchange at 323 K for 30 min (Table 2), using a molar extinction coefficient of 2×10^6 cm/mol [17].

3.3. Pd characterization

For n-C_{16} hydrocracking activity, the samples were loaded with ~1.0 wt% Pd (Table 2). The atomic Pd/H^+ ratios were between 1.6 and 82.2, indicating that there should be enough metal function to ensure an appropriate supply of olefins to the acid sites and to establish acid-catalyzed isomerization and cracking reactions as the rate-limiting steps [45,46]. The dispersion of the Pd metal phase was determined by H_2 chemisorption (i.e., the ratio between irreversibly adsorbed hydrogen (H_{irr}) and the total amount of Pd [47]). We assumed a $H_{irr}/Pd_s = 1$ stoichiometry for the Pd nanoparticles [48]. The Pd dispersion is below 0.5 for all samples and Pd/ASA exhibits the lowest Pd dispersion. The Pd particle size distribution was determined in more detail by TEM for the SBA-15 and MCM-41/MCM-48 samples (Fig. S2). Relatively uniformly sized Pd particles were observed for these samples with average sizes ranging from 3.0 ± 0.7 nm for sample P1.7 to 11.3 ± 3.4 nm for P1.6. Based on the average pore size determined by Ar porosimetry, we estimate the fraction of Pd particles located inside the mesopores. For SBA-15, the majority of Pd particles have sizes smaller than the pore size (Table S1), except for P1.5 and P1.6 for which only, respectively, 15% and 30% of the Pd particles are smaller than the pore size. On the contrary, the Pd particles in the M41–40, M41–60 and M48–60 sample are mostly larger than the mesopores, indicating that most of the Pd particles are located on the external surface of the M41S silicas.

We also studied by IR spectroscopy the adsorption of CO on metallic Pd at 303 K. Before CO dosing, the samples were reduced at 673 K and evacuated to a pressure lower than 10^{-5} mbar. An example spectrum of CO adsorbed on sample P1.7 (Fig. S4) shows a broad low-frequency signal between 1700 and 2000 cm^{-1} and a high-frequency signal between 2000 cm^{-1} and 2150 cm^{-1}, generally assigned to CO bridged and linear chemisorbed to Pd, respectively [49]. Deconvolution of the IR bands was carried out following literature [50]. The peak at 1895 cm^{-1} has been attributed to μ_2-bridge-bonded CO on the (100) plane of Pd [51]. The 1930 cm^{-1} peak is due to μ_2-bridge-bonded CO on (111) planes and the ones at 1961 cm^{-1} and 1976 cm^{-1} relates to bridge-bonded CO on Pd particle edges and steps [52,53]. The signal located at 2074 cm^{-1} is assigned to linear CO bound to (111)/(111) and (111)/(100_ edges sites and the one at 2091 cm^{-1} is due to CO residing on corner Pd atoms [50]. Bridge-to-linear adsorbed CO molar ratios (B/L)

Table 2
Concentration of BAS, Pd content, Pd/H^+ molar ratio, Dispersion and B/L molar ratio.

Sample	BAS, CO IR (μmol/g)[a]	BAS, pyridine IR (μmol/g)[b]			BAS, H/D exchange (μmol/g)[c]	Pd loading (wt%)[d]	Pd/H^+[e]	Pd dispersion[f]	Pd particle size[g]	B/L[h]
		423 K	573 K	773 K						
P1.0	0	0	0	0	0	–	–	–	–	–
P1.5	2	22	9	0	0.2	0.97	82.2	0.18	11.3 ± 2.9	0.31
P1.6	4	55	17	0	1.1	0.89	20.6	0.27	11.3 ± 3.4	0.21
P1.7	3	72	16	0	2.0	1.01	4.4	0.09	3.0 ± 0.7	0.44
P2.0	5	87	19	0	5.3	1.18	8.3	0.39	6.6 ± 2.1	0.11
P2.5	6	89	30	0	5.5	1.04	7.4	0.42	4.8 ± 1.4	0.04
M41–40	2	63	21	0	2.6	0.98	8.2	0.23	8.0 ± 1.9	0.25
M41–60	3	73	28	0	4.5	0.86	3.7	0.20	6.2 ± 1.5	0.28
M48–60	6	97	29	0	1.2	1.06	12.1	0.15	9.7 ± 3.8	0.30
ASA	4	66	45	0	4.3	0.96	1.6	0.08	n.d.	0.45

[a] From the peak at 2177 cm^{-1}.
[b] From the peak at 1545 cm^{-1}.
[c] Sum of peaks at 2632 $cm^{-1}$and 2683 cm^{-1}.
[d] Determined by ICP.
[e] Ratio of Pd surface sites and BAS; Pd surface sites from H_2 chemisorption, BAS from H/D exchange IR.
[f] H/Pd ratio based on H_2 chemisorption and Pd metal loading.
[g] From TEM measurements.
[h] Bridge-to-linear ratio of CO adsorbed on the metallic Pd phase.

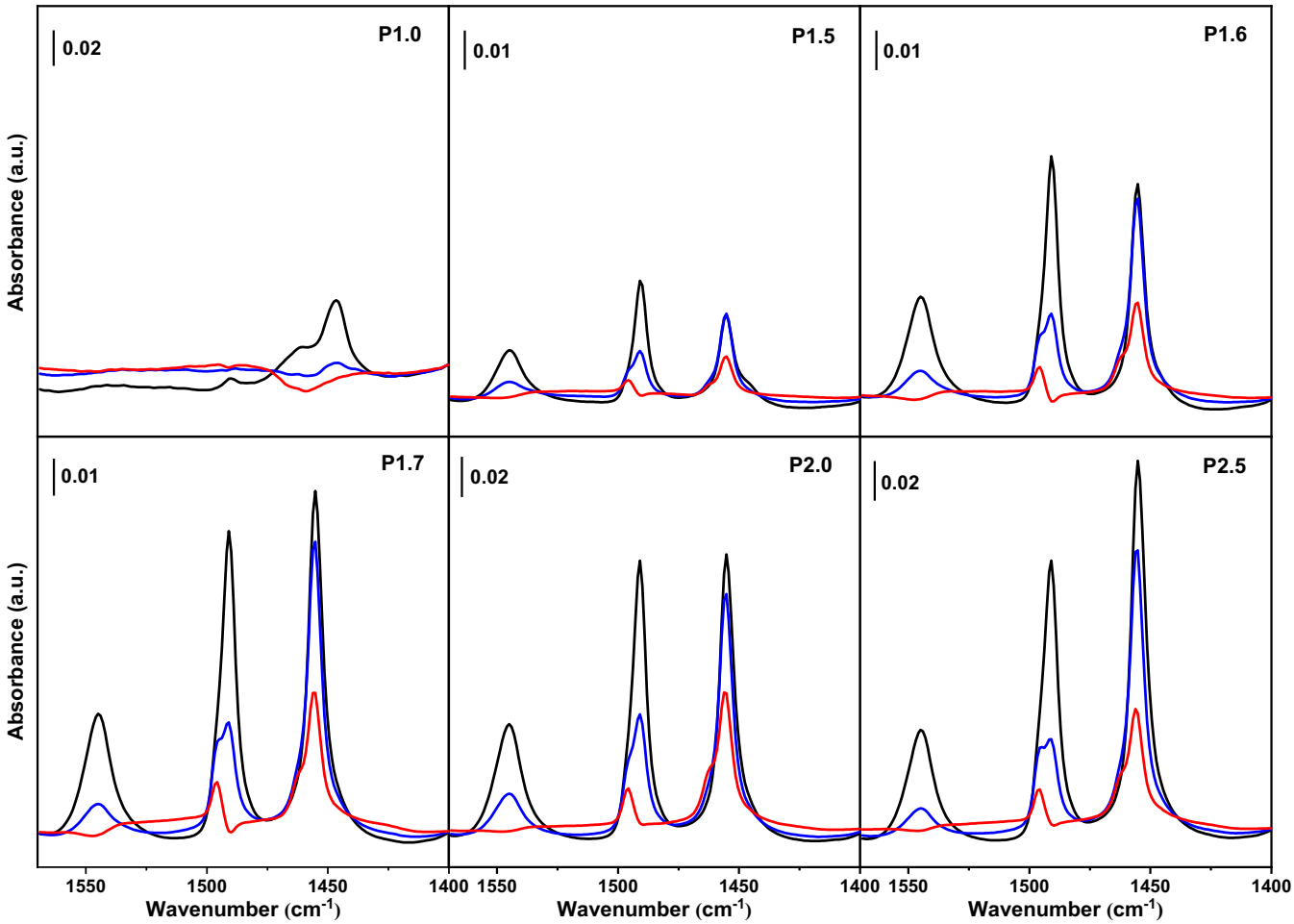

Fig. 6. IR spectra of pyridine adsorbed on SBA-15 samples after evacuation at 423 K (black line), 573 K (blue line) and 773 K (red line). All spectra were recorded at 423 K. (For interpretation of the references to colour in this figure legend, the reader is referred to the web version of this article.)

calculated after saturation with CO are presented in Table 2 using molar extinction coefficients of 4.1×10^6 cm/mol (bridge species) and 0.36×10^6 cm/mol from literature [54]. B/L values are in line with the dispersion trend following from H_2 chemisorption, i.e., samples with high dispersion present a lower amount of CO bound on bridge sites.

3.4. Catalytic activity

The hydroconversion of n-C_{16} was carried out at a weight hourly velocity of 10 $g_{n\text{-}C16}\ g_{cat}^{-1}\ h^{-1}$, a total pressure of 60 bar and a H_2/n-C_{16} ratio of 20. The n-C_{16} conversion for the investigated samples is shown as a function of the temperature in Fig. 8. For all sample families with the exception of M41–40, the activity correlates with the Al content.

The apparent activation energies fall in the range of 169–220 kJ/mol, which is higher than typical values for catalysts containing amorphous silica-alumina as the acidic component [55]. Both skeletal isomers and cracked alkanes were obtained as reaction products (Fig. S5). Overall, the highest isomers yield was obtained for the ASA-based catalyst. For the SBA-15 catalysts, the isomers yields were very similar as a function of conversion with the exception of P1.7, which presented a much lower isomers yields (more cracking). The other samples presented lower isomers yields in the order M41–40 ≈ M41–60 > M48–60.

Fig. 9 (Fig. S5) shows the molar ratio between cracked (C) and total (T) products extrapolated to zero n-C_{16} conversion [56,57], denoted by the parameter $(C/T)_{x\to 0}$, as a function of Al content. In ideal hydrocracking and at low conversion, monobranched isomers should be dominant products without formation of cracking products, i.e., $(C/T)_{x\to 0}$ should approach zero. There is a strong relation between the initial formation of cracked products and the structure of the materials. $(C/T)_{x\to 0}$ decreases with increasing Al content for the SBA-15 samples. This is counterintuitive, because hydrocracking is expected to be ideal for low acidity materials. The observed trend cannot be directly related to the Pd dispersion (cf. Table 2). Instead, we attribute the decreasing cracking tendency with increasing Al content to the loss of order of mesopores in these samples. The lowest $(C/T)_{x\to 0}$ values are obtained for the disordered samples prepared at a pH of 2 or higher. A similar trend with respect to pore ordering can be observed for the MCM-41/MCM-48 catalysts. Especially, the catalyst presenting long cylindrical pores (M41–60) exhibits higher $(C/T)_{x\to 0}$ than M48–60 with interconnected channels. This behavior, which is likely enhanced by the low Pd dispersion of the latter sample, relates to the longer residence of olefinic intermediate in one-dimensional ordered pore systems, resulting in enhanced cracking. Partial disorder of the mesopores will decrease the diffusion length inside these pores. We further investigated whether improving the metal function would affect the product distribution. For this purpose, we added 0.5 wt% Pt to the P1.7 sample by a follow-up impregnation procedure using an aqueous $H_2PtCl_6{*}6H_2O$ solution and calcination at 723 K in flowing air for 4 h. This catalyst is denoted as P1.7(+Pt) in Fig. 10. For this sample, the $(C/T)_{x\to 0}$ ratio decreased to the same values obtained for the disordered materials prepared at higher pH, indicating that in the original P1.7 sample the metal function was not strong enough relative to the diffusion lengths.

Fig. 10 shows the n-C_{16} conversion as a function of temperature for the P1.7 and P1.7(+Pt) samples. It can be observed that the addition of

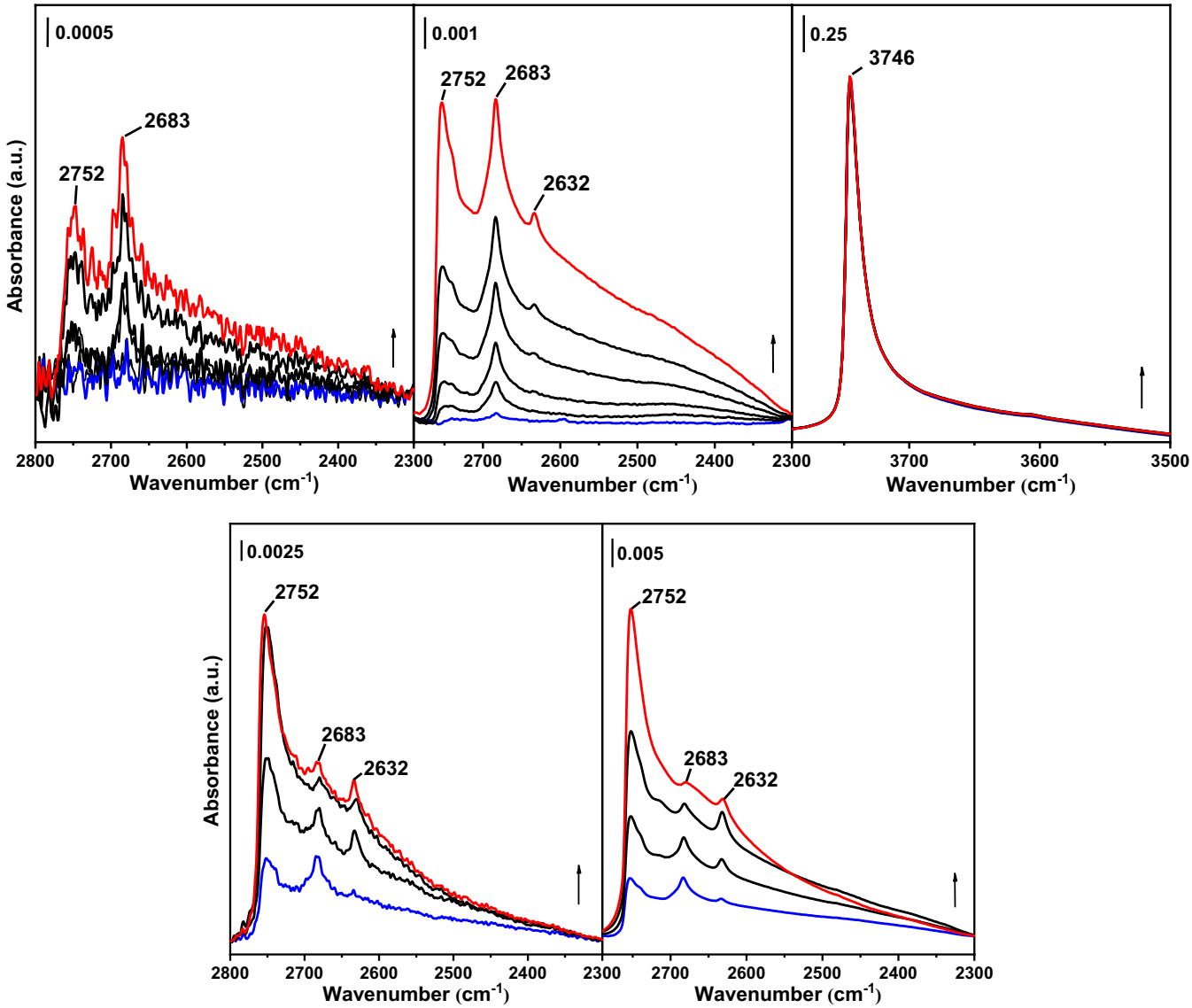

Fig. 7. IR spectra in the OD region of M48–60 (top, left) and P1.7 (top, center), and in the OH region of P1.7 (top, right) after H/D exchange for increasing exposure times (10 s, 30 s, 300 s, 600 s, 1200 s, 1800 s) at 303 K. FTIR spectra in the deuteroxyl region of M48–60 (bottom, left) and P1.7 (bottom, right) for increasing temperatures (323 K, 353 K, 373 K and 423 K) and 1800 s.

Pt results in a significantly higher n-C_{16} conversion. The apparent activation energy was lowered from 220 kJ/mol to 154 kJ/mol, approaching the values reported in the literature [55]. Together with the much higher isomers yields observed for P1.7(+Pt), we conclude that the performance of P1.7 was limited by the metal function. We also estimated the average number of acid-catalyzed steps involved in n-C_{16} hydroconversion extrapolated to zero conversion ($n_{as,\ x\to 0}$, Table S1), considering the selectivity of monobranched/multibranched isomers and cracked products. It takes one acid-catalyzed step to form monobranched isomers, 2 and 3 for dibranched and tribranched isomers, respectively, and typically 4 for cracking. Therefore, $n_{as,\ x\to 0}$ would approach unity for an ideal hydrocracking catalyst. Conversely, a catalyst operating outside this regime, i.e. with a poor balance of hydrogenation and cracking sites or presenting severe shape selectivity effects will present higher $n_{as,\ x\to 0}$ values, indicating consecutive isomerization and cracking of the more reactive multibranched isomers already at low conversion [57]. Values of $n_{as,\ x\to 0}$ around 1.4 and 1.6 seem to indicate that the samples do not suffer from shape selectivity or a poor metal/acid balance. Nevertheless, the values are slightly higher for the samples with ordered mesopores.

We also observed that the distribution of monobranched isomers at low and 50% n-C_{16} conversion is very similar for all samples (Fig. S6). At both conversion levels, the product distribution is dominated by 7-methylpentadecane (7-meC_{15}) and 8-methylpentadecane (8-meC_{15}) with lower amounts of other isomers. At a n-C_{16} conversion of 50%, nonetheless, the amounts of 7-meC_{15} and 8-meC_{15} are less pronounced and the concentration of other isomers increases.

The product distribution of cracked hydrocarbons is plotted in Fig. 11. Samples supported on supports with a well-ordered mesopore structure present higher cracking selectivity than samples with a disordered mesopore structure (i.e., ASA, M41–40, P2.0 and P2.5). In general, all Pd-loaded catalysts exhibit an asymmetric distribution of cracked products shifted to lighter products with C_4-C_6 being the dominant products. Cracking is more substantial for samples with ordered mesopores in comparison with samples having disordered pore systems. Adding Pt to P1.7 also leads to a lower degree of cracking and a cracked product distribution corresponding more to the one expected for ideal hydrocracking. These differences suggest that some degree of

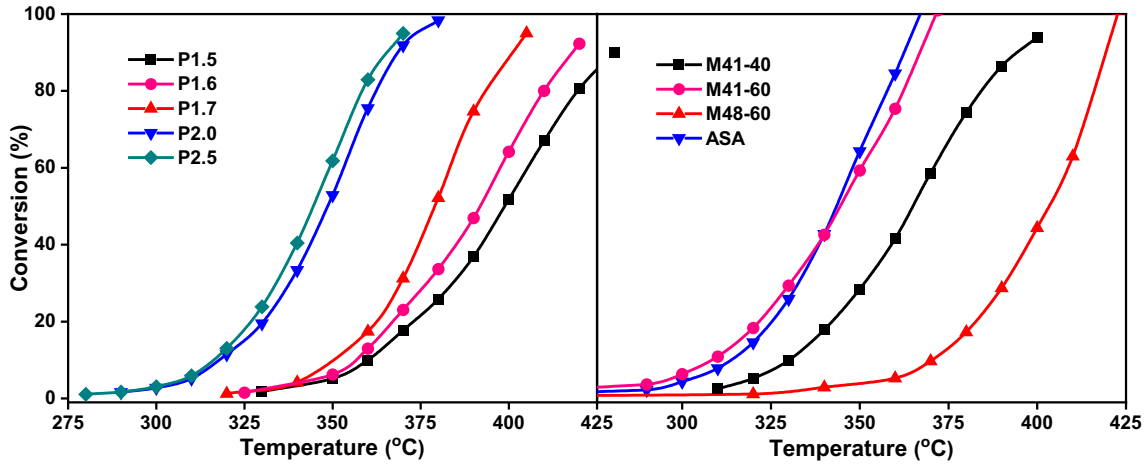

Fig. 8. Conversion of n-hexadecane as a function of the reaction temperature for SBA-15 (left) and MCM-41/MCM-48 catalysts (WHSV = 10 $g_{n\text{-}C16}\ g_{cat}^{-1}\ h^{-1}$, H_2/n-hexadecane = 20, P = 60 bar,~ 1 wt% Pd).

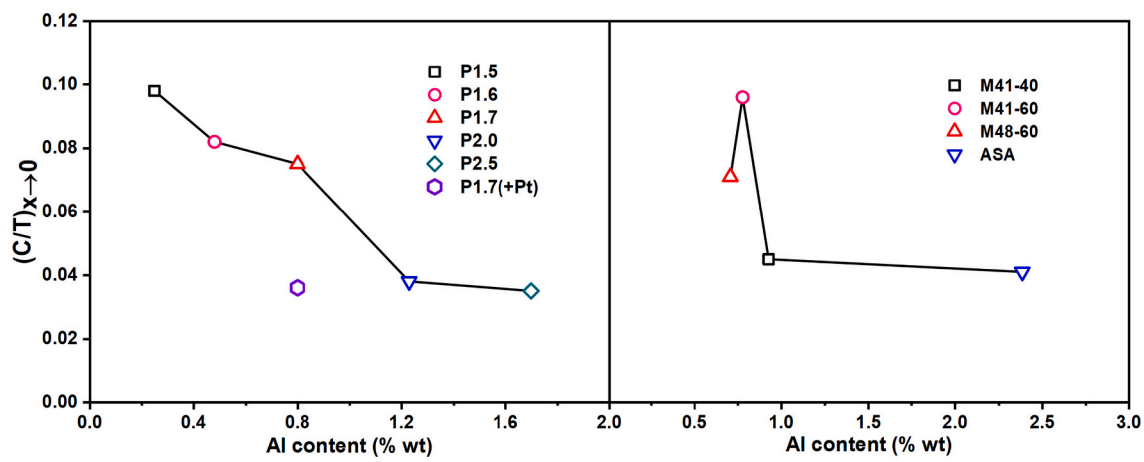

Fig. 9. Molar ratio between cracking and total products extrapolated to zero conversion, $(C/T)_{x\to 0}$, in the hydrocracking of n-C_{16} of SBA-15 (left) and MCM-41/MCM-48 (right) catalysts (WHSV = 10 $g_{n\text{-}C16}\ g_{cat}^{-1}\ h^{-1}$, H_2/n-hexadecane = 20, P = 60 bar,~ 1 wt% Pd).

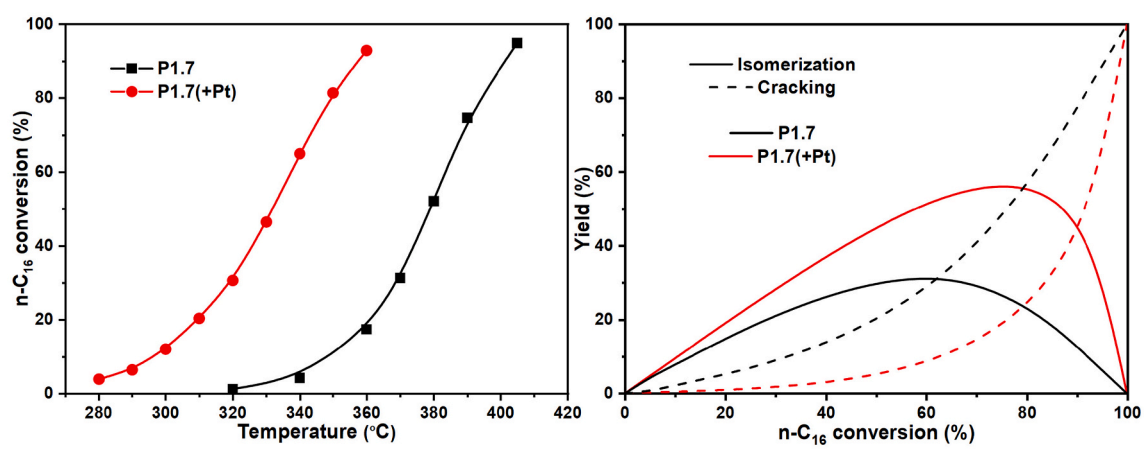

Fig. 10. Conversion of n-hexadecane as a function of the reaction temperature (left) and product yield distribution as a function of n-hexadecane conversion (right) for P1.7 and P1.7(+Pt) catalysts.

secondary cracking takes place, which associated with an increased residence time of the olefinic intermediates as discussed previously [58]. It is evident from the results that, in the case the metal hydrogenation function is not strong enough, the product distribution is influenced not only by the order of the pores, but also by the concentration of acid sites. The occurrence of secondary cracking suggests that the diffusion of

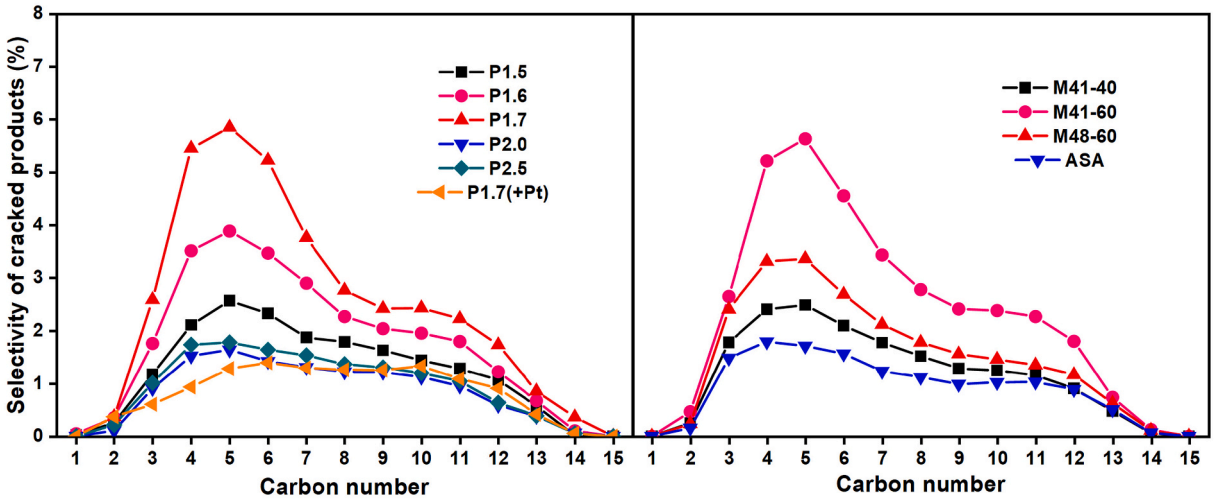

Fig. 11. Selectivity of cracked products obtained at ca. 50% n-hexadecane conversion.

hydrocarbons plays an important role in the reaction mechanism, especially inside the long cylindrical pores of SBA-15 and MCM-41 based catalysts [59].

It appears also that the addition of Pt as a stronger hydrogenation function can also impact the product distribution. The observation that Pt addition also increases the overall n-C_{16} conversion implies that the dehydrogenation function of P1.7 is not strong enough. This may be because Pt presents a stronger hydrogenation activity or Pt is more readily dispersed than Pd. While this may be due to the low Pd dispersion in the P1.7 sample, this result shows that a too low hydrogenation function leads to overcracking in 1-dimensional mesopores. Wang et al. earlier showed the sensitivity of the product distribution on the location, size and shape of Pt nanoparticles [60].

4. Conclusions

In this work we obtained insight into the role of size and order of the pores of (ordered) mesoporous silica (SBA-15, M41S and ASA) on the bifunctional hydrocracking of n-hexadecane. A series of Al-modified ordered mesoporous SBA-15, MCM-41 and MCM-48 and disordered ASA were employed as the acid component for the bifunctional catalysts, which were also loaded with Pd as the hydrogenation component. SBA-15 materials were prepared at different pH, which was found to simultaneously influence the Si/Al ratio and order of mesopores. Al was introduced in MCM-41 and MCM-48 by a post-synthesis grafting method. All materials including ASA exhibited low acidity compared to zeolites. A general trend is that increasing Al incorporation (alumination for M41S, higher pH synthesis for SBA-15) led to a loss of ordering of the mesopores. The Pd metal phase was Pd sites homogeneously dispersed as ~10 nm particles. In n-C_{16} hydroconversion, it was observed that secondary cracking is more pronounced for catalysts containing long one-dimensional cylindrical pores (SBA-15 and MCM-41) than for catalysts containing a three-dimensional ordered or disordered mesoporous texture, which can be attributed to the difference in residence time of intermediates in the mesopores. From the observation that secondary cracking increased for lower Pd dispersion, it is inferred that the distance of acid sites in the mesopores and the metal phase mainly located outside these pores also plays a role. This was further corroborated by adding Pt to a mesoporous Pd/SBA-15 sample, which improved the overall catalytic activity and decreased secondary cracking reactions. Ideal hydrocracking operation is approached for ASA, MCM-48, and SBA-15 prepared at a high pH with a disordered mesopore system.

Declaration of Competing Interest

The authors declare that they have no known competing financial interests or personal relationships that could have appeared to influence the work reported in this paper.

Acknowledgements

This research was financially supported by Shell Global Solutions International B.V. The authors thank A.M. Elemans-Mehring for ICP-OES analysis and the Soft Matter Cryo-TEM Research Unit of Eindhoven University of Technology for access to TEM facilities. The authors thank Arno van Hoof, Tobias Kimpel and Jiadong Zhu for TEM analyses.

Appendix A. Supplementary data

Supplementary data to this article can be found online at https://doi.org/10.1016/j.fuproc.2022.107259.

References

[1] J. Weitkamp, H. Schulz, J. Catal. 29 (1973) 361–366.
[2] P.B. Weisz, Adv. Catal. 13 (1962) 137–190.
[3] T.F. Degnan, C.R. Kennedy, AICHE J. 39 (1993) 607–614.
[4] D.S. Santilli, T.V. Harris, S.I. Zones, Microporous Mater. 1 (1993) 329–341.
[5] J. Weitkamp, ChemCatChem 4 (2012) 292–306.
[6] M.J. Girgis, Y.P. Tsao, Ind. Eng. Chem. Res. 35 (1996) 386–396.
[7] J. Jiang, C. Yang, Z. Lu, J. Ding, T. Li, Y. Lu, F. Cao, Catal. Commun. 60 (2015) 1–4.
[8] R. de Haan, G. Joorst, E. Mokoena, C.P. Nicolaides, Appl. Catal. A Gen. 327 (2007) 247–254.
[9] P. Selvam, S.K. Bhatia, C.G. Sonwane, Ind. Eng. Chem. Res. 40 (2001) 3237–3261.
[10] D. Zhao, J. Feng, Q. Huo, N. Melosh, G.H. Fredrickson, B.F. Chmelka, G.D. Stucky, Science (80-.). 279 (1998) 548–552.
[11] D. Zhao, Q. Huo, J. Feng, B.F. Chmelka, G.D. Stucky, J. Am. Chem. Soc. 120 (1998) 6024–6036.
[12] Y. Li, W. Zhang, L. Zhang, Q. Yang, Z. Wei, Z. Feng, C. Li, J. Phys. Chem. B 108 (2004) 9739–9744.
[13] W. Sangchoom, R. Mokaya, J. Mater. Chem. 22 (2012) 18872.
[14] Y. Xia, R. Mokaya, J. Mater. Chem. 13 (2003) 657–659.
[15] R. Mokaya, 8 (2002) 360–363.
[16] Y. Xia, R. Mokaya, J. Phys. Chem. C 112 (2008) 1455–1462.
[17] E.J.M. Hensen, D.G. Poduval, D.A.J.M. Ligthart, J.A.R. van Veen, M.S. Rigutto, J. Phys. Chem. C 114 (2010) 8363–8374.
[18] M.C. Claude, G. Vanbutsele, J.A. Martens, J. Catal. 203 (2001) 213–231.
[19] W. Li, S.J. Huang, S.B. Liu, M.O. Coppens, Langmuir 21 (2005) 2078–2085.
[20] S.A. Bagshaw, E. Prouzet, T.J. Pinnavaia, Science (80-.). 269 (1995) 1242–1244.
[21] C.G. Goltner, M. Antonietti, Adv. Mater. 9 (1997) 431–436.
[22] Q. Huo, D.I. Margolese, G.D. Stucky, Chem. Mater. 8 (1996) 1147–1160.
[23] J.P. Lourenço, A. Fernandes, C. Henriques, M.F. Ribeiro, Microporous Mesoporous Mater. 94 (2006) 56–65.
[24] H. Kosslick, G. Lischke, B. Parlitz, W. Storek, R. Fricke, Appl. Catal. A Gen. 184 (1999) 49–60.

[25] K.N. Tayade, M. Mishra, J. Mol. Catal. A Chem. 382 (2014) 114–125.
[26] H. Liu, G. Lu, Y. Guo, Y. Wang, Y. Guo, J. Colloid Interface Sci. 346 (2010) 486–493.
[27] M. Kruk, M. Jaroniec, Chem. Mater. 15 (2003) 2942–2949.
[28] J.T. Tompkins, R. Mokaya, ACS Appl. Mater. Interfaces 6 (2014) 1902–1908.
[29] K. Schumacher, P.I. Ravikovitch, A. Du Chesne, A.V. Neimark, K.K. Unger, Langmuir 16 (2000) 4648–4654.
[30] J.-H. Sun, M.-O. Coppens, J. Mater. Chem. 12 (2002) 3016–3020.
[31] J.M. Kim, M. Kruk, M. Jaroniec, R. Ryoo, Chem. Mater. 11 (1999) 2568–2572.
[32] M.L. Ojeda, J.M. Esparza, A. Campero, S. Cordero, I. Kornhauser, F. Rojas, Phys. Chem. Chem. Phys. 5 (2003) 1859–1866.
[33] Z. Luan, C.F. Cheng, W. Zhou, J. Klinowski, J. Phys. Chem. 99 (1995) 1018–1024.
[34] B. Li, X. Li, J. Xu, X. Pang, X. Gao, Z. Zhou, J. Colloid Interface Sci. 346 (2010) 199–207.
[35] V. Alfredsson, M.W. Anderson, Chem. Mater. 8 (1996) 1141–1146.
[36] C. Hernandez, A.C. Pierre, Langmuir 16 (2000) 530–536.
[37] G. Crépeau, V. Montouillout, A. Vimont, L. Mariey, T. Cseri, F. Maugé, J. Phys. Chem. B 110 (2006) 15172–15185.
[38] E.J.M. Hensen, D.G. Poduval, V. Degirmenci, D.A.J. Ligthart, W. Chen, F. Maugé, M.S. Rigutto, J.A.R. Van Veen, J. Phys. Chem. C 116 (2012) 21416–21429.
[39] O. Cairon, T. Chevreau, J.C. Lavalley, J. Chem. Soc. Faraday Trans. 94 (1998) 3039–3047.
[40] W. Daniell, N.-Y. Topsøe, H. Knozinger, Langmuir 17 (2001) 6233–6239.
[41] X. Zhu, L. Wu, P.C.M.M. Magusin, B. Mezari, E.J.M. Hensen, J. Catal. 327 (2015) 10–21.
[42] C.A. Emeis, J. Catal. 141 (1993) 347–354.
[43] H.G. Karge, Microporous Mesoporous Mater. 22 (1998) 547–549.
[44] D.G. Poduval, J.A.R. van Veen, M.S. Rigutto, E.J.M. Hensen, Chem. Commun. (Camb.) 46 (2010) 3466–3468.
[45] G.E. Giannetto, G.R. Perot, M.R. Guisnet, Ind. Eng. Chem. Prod. Res. Dev. 25 (1986) 481–490.
[46] M. Guisnet, F. Alvarez, G.E. Giannetto, G.R. Perot, Catal. Today 1 (1987) 415–433.
[47] M.A. Aramendia, V. Borau, C. Jimenez, J.M. Marinas, A. Moreno, Colloids Surf. A Physicochem. Eng. Asp. 106 (1996) 161–165.
[48] G. Prelazzi, M. Cerboni, G. Leofanti, J. Catal. 181 (1999) 73–79.
[49] Y. Soma-Noto, W.M.H. Sachtler, J. Catal. 32 (1974) 315–324.
[50] A.M. Venezia, L.F. Liotta, G. Deganello, P. Terreros, M.A. Peña, J.L.G. Fierro, Langmuir 15 (1999) 1176–1181.
[51] T. Lear, R. Marshall, J.A. Lopez-Sanchez, S.D. Jackson, T.M. Klapötke, M. Bäumer, G. Rupprechter, H.J. Freund, D. Lennon, J. Chem. Phys. 123 (2005) 1–13.
[52] A. Palazov, C.C. Chang, R.J. Kokes, J. Catal. 36 (1975) 338–350.
[53] L.F. Liotta, G.A. Martin, G. Deganello, J. Catal. 164 (1996) 322–333.
[54] M.A. Vannice, S.Y. Wang, J. Phys. Chem. 85 (1981) 2543–2546.
[55] I. Rossetti, C. Gambaro, V. Calemma, Chem. Eng. J. 154 (2009) 295–301.
[56] N. Batalha, L. Pinard, C. Bouchy, E. Guillon, M. Guisnet, J. Catal. 307 (2013) 122–131.
[57] N. Batalha, L. Pinard, Y. Pouilloux, M. Guisnet, Catal. Lett. 143 (2013) 587–591.
[58] J. Weitkamp, P.A. Jacobs, J.A. Martens, Appl. Catal. 8 (1983) 123–141.
[59] R. Krishna, J. Phys. Chem. C 113 (2009) 19756–19781.
[60] Y. Wang, Z. Tao, B. Wu, J. Xu, C. Huo, K. Li, H. Chen, Y. Yang, Y. Li, J. Catal. 322 (2015) 1–13.